ABSTRACT

Title of dissertation:	Direct measurement of a Feshbach resonance with imaging and measuring topology of BECs in a synthetic dimensions
	Dina Genkina Doctor of Philosophy, 2018
Dissertation directed by:	Professor Ian Spielman Department of Physics

Direct measurement of a Feshbach resonance with imaging of s-wave
scattering
and measuring topology of BECs in a synthetic dimensions lattice

by

Dina Genkina

Dissertation submitted to the Faculty of the Graduate School of the
University of Maryland, College Park in partial fulfillment
of the requirements for the degree of
Doctor of Philosophy
2018

Advisory Committee:
Professor Ian Spielman, Chair/Advisor

Chapter 2: Absorption imaging in the presence of strong recoil induced detuning

2.1 Near-resonant atom-light interaction

In this section, we will assume the atom can be treated as a two-level system: one with a ground and excited atomic state, with an energy difference of energy difference $\hbar\omega_0$. When such an atom, starting in the ground state, is illuminated by a laser beam with frequency $\hbar\omega_L$, there are three kinds of transitions that occur: during aborption the atom aborbs a photon from the laser and goes from the ground to the excited state; during stimulated emission, the atom emits a photon into the field of the laser beam and jump from the excited to the ground state; during spontaneous emission, the atom decays to the ground state from the excited state with no help from the laser, emitting into a random vacuum mode. Stimulated emission results in coherent light co-propagating with the laser beam, while spontaneous emission results in light scattering incoherently in any direction. The rate of spontaneous emission from an excited state is given by the natural transition linewidth of the transition Γ.

On timescales short compared to $1/\Gamma$, spontaneous emission can be ignored, and an atom undergoes coherent Rabi oscillations between the ground and excited states via cycles of absorption and stimulated emission [1]. Taking c_g and c_e to be the time-dependent coefficients multiplying the eigenstate wavefuntions of the ground and excited state respectively, and assuming the atom starts in the ground

state $c_g(t = 0) = 1$, the excited state population is given by

$$c_e(t) = -i\frac{\Omega}{\Omega'}sin\left(\frac{\Omega't}{2}\right)e^{-i\delta t/2}, \qquad (2.1)$$

where Ω is the Rabi frequency given by $SOMETHINGINTERMSOFINTENSITY$, $\Omega' = \sqrt{\Omega^2 + \delta^2}$ is the generalized Rabi frequency and $\delta = \omega_0 - \omega_L$ is the detuniong of the laser from atomic resonance.

In the regime where spontaneous emission cannot be ignored, Rabi oscillations of each individual atom are intermittently interrupted by decay to the ground state. Averaging over an atomic ensamble, on the time scale of a single Rabi oscillation the overall excited state population reaches a steady state, and the rate of spontaneous emission becomes constant. Since during spontaneous emission the ejected photon can go into any vacuum mode, this process can be thought of as the scattering of photons by the atoms. This scattering rate is given by [1]

$$\gamma_{sc} = \frac{\Gamma}{2}\frac{I/I_{sat}}{1 + 4(\delta/\Gamma)^2 + I/I_{sat}}, \qquad (2.2)$$

where I_{sat} is the saturation intensity. This is the intensity at which the timescale of spontaneous emission matches the Rabi oscillation rate, reducing the capacity for absorption of extra light.

2.2 Absorption imaging

Absorption imaging takes advantage of the on-resonant interaction described in the previous section. An on or near-resonant laser beam $(\delta/\Gamma \ll 1)$ is shined at the atoms, and the aborbed light acts to create a shadow in the shape of the atoms in the laser beam. This beam with the shadow is then imaged on a camera, in our case a CCD, as depicted in Figure 1a (top). This is called the atom image,

and the intensity distribution over the camera is denoted by $I_f(x, y)$, where the subscript f stands for final - the intensity after the light has encountered the atoms. To quantify the 'shadowed out' intensity, after the atoms have left the trap the same laser intensity is shined directly at the camera, as in Figure 1a (bottom). This is called the probe image, and the intensity distribution over the camera is denoted by $I_0(x, y)$, where the subscript 0 indicated initial - the intensity before the light had encountered the atoms.

To recover the atom number distribution encountered by the light, consider an atomic cloud with 3D density $\rho(x, y, z)$. Since we can only obtain 2D information from the camera, we can only hope to recover a 2D atomic column density $n(x, y) = \int \rho(x, y, z) \mathrm{d}z$. Focusing in on a single pixel of the camera, we can consider a single value of I_0 and I_f to recover a local n. As the laser light propagates through the atomic cloud, the intensity of the light will diminish due to absorption. This absorption as a function of propagation direction z can be expressed using the scattering rate equation Eq. 2.2 as the number of photons scattered by the atoms (proportional to the atomic density times the scattering rate) times the photon energy $\hbar\omega_\mathrm{L}$:

$$\frac{d}{dz}\frac{I(z)}{I_\mathrm{sat}} = -\hbar\omega_\mathrm{L}\rho(z)\gamma_{sc}(z) = -\rho(z)\sigma_0\frac{I(z)/I_\mathrm{sat}}{1 + 4\delta^2/\Gamma^2 + I(z)/I_\mathrm{sat}}, \qquad (2.3)$$

where the resonant scattering cross section is $\sigma_0 = 3\lambda_0^2/2\pi$, and λ_0 is the wavelength asociatted with atomic resonance.
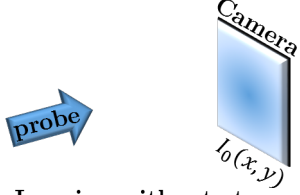
Integrating both sides of Eq. 2.3, we obtain

$$\sigma_0 n = \left(1 + 4\delta^2/\Gamma^2\right)\ln(I_0/I_f) + (I_0 - I_f)/I_\mathrm{sat}. \qquad (2.4)$$

The quantity $OD = ln(I_0/I_f)$ is called the optical depth of the cloud. When the probe intensity I_0 is much smaller than the saturation intensity, the second term in
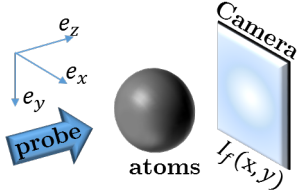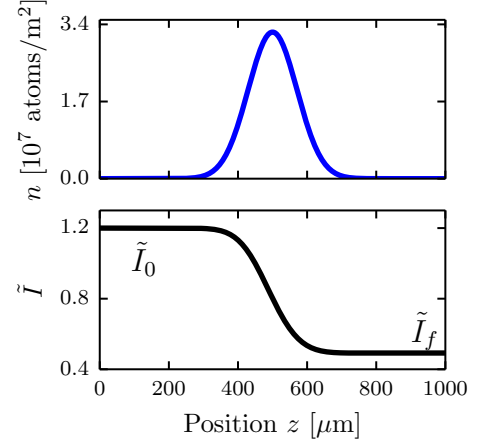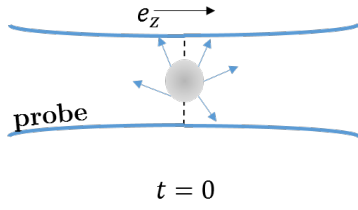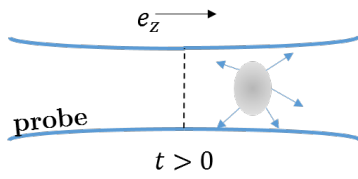
Figure 1: Absorption imaging. (a) Near resonant probe light illuminates the atoms, and the transmitted light (containing a shadow of the atoms) is imaged on the camera. A second image taken with no atoms provides a reference. (b) The probe beam is partially absorbed as it traverses the cloud, and the intensity seen by atoms further along the imaging direction $e_{\mathbf{z}}$ is lowered. (c) An atomic cloud illuminated by a probe light field absorbs photons from the probe and re-emits them in all directions. This process results in a net acceleration of the cloud in the direction of the probe light as well as diffusive spreading in the transverse directions.

Eq. 2.4 becomes negligible. Assuming further that the probe light is on resonance, $\delta = 0$, the atomic column density becomes simply $\sigma_0 n = OD$. Figure 1b shows a Gaussian atomic density distribution (top) and the resulting probe intensity as a function of position in the cloud (bottom). The intensity drops from its initial to final value gradually as it traverses the cloud.

However, there is an important effect that the above equations do not account for. Namely, as the atoms absorb light from the probe beam, they also get a momentum kick equal to the momentum of a photon during each collision $\hbar k_r = h/\lambda_L$ in the direction of propagation. It is true that the absorbed photon will then be re-emitted by the atom, inducing a loss of momentum, but since this happens through the process of spontaneous emission into a random vacuum mode, the average momentum kick acquired this way over many re-emissions will average to zero. On average, each photon absorbed will induce a change in velocity of the atom of $v_r = \hbar k_r/m$, where m is the atomic mass, as depicted in Fig. 1c. As the velocity of the atom changes, due to the Doppler effect, the apparent laser frequency will change as well. Therefore, even if the laser light is exactly on-resonant for a stationary atom, it will become off-resonant for longer imaging times, and Eq. 2.3 will acquire a time dependence. For most experiments, this effect is small and can be neglected. However, if the imaging time becomes of order a recoil time t_r, a time after which the recoil-induced detuning δ becomes of order Γ, this effect becomes significant. We explore this effect in the following sections.

2.3 Recoil-induced detuning

After absorbing a number of photons N, an atom will obtain a recoil velocity of $N v_r$. Via the Doppler effect, this will result in a detuning $\delta = N k_r v_r$. This detuning will increase as more atoms are absorbed, and therefore depend on time, making the absorbed intensity also time dependent. We can generalize Eq. 2.3 to

include a time dependence on the detuning term and therefore also the intensity:

$$\frac{d}{dz}\frac{I(z,t)}{I_{\text{sat}}} = -\rho(z)\sigma_0\frac{I(z,t)/I_{\text{sat}}}{1 + 4\delta(z,t)^2/\Gamma^2 + I(z,t)/I_{\text{sat}}}. \tag{2.5}$$

The number of photons absorbed per atom will depend on the intensity lost, up until the current time, at that location. The detuning will therefore be proportional to the total number of photons lost up until time t at that location, proportional to the absorbed intensity divided by the single photon energy $\hbar\omega_L$, divided by the number of atoms that participated in the aborption $\rho(z)$ times the detuning $k_{\text{r}}v_{\text{r}}$:

$$\delta(t,z) = \frac{k_{\text{r}}v_{\text{r}}}{\hbar\omega_L\rho(z)}\int_0^t\frac{dI(z,\tau)}{dz}\mathrm{d}\tau. \tag{2.6}$$

These equations are interdependent, and cannot be in general solved analytically.

Figure 2a shows the velocity and detuning as a function of position in space for three different imaging times, calculated numberically. All calculations in this chapter were done for a cloud of ^{4}0K atoms, as that is relevant to our experiment described in the next chapter. The resonant wavelength is $PUTALLNUMBERSFORKINHERE$

2.4 Perturbative treatment

We can treat these equations perturbatively in time. To first order, we can set the detuning in Eq. 2.5 to $\delta = 0$, assume $I(z)$ is time independent, and plug that into Eq. 2.6 to obtain

$$\delta(t,z) = \frac{k_{\text{r}}v_{\text{r}}}{\hbar\omega_L\rho(z)}\int_0^t -\rho(z)\sigma_0\frac{I(z)}{1 + I(z)/I_{\text{sat}}}\mathrm{d}\tau \tag{2.7}$$

$$= \frac{k_{\text{r}}v_{\text{r}}\sigma_0}{\hbar\omega_L}\frac{I(z)}{1 + I/I_{\text{sat}}}t. \tag{2.8}$$

This can then be recursively plugged into Eq. 2.5 to obtain

$$\frac{d}{dz}\frac{I(z,t)}{I_{\text{sat}}} = -\rho(z)\sigma_0 \frac{I(z,t)/I_{\text{sat}}}{1 + 4\left(\frac{k_{\text{r}}v_{\text{r}}\sigma_0}{\hbar\omega_L\Gamma}\frac{I(z)}{1+I/I_{\text{sat}}}\right)^2 t^2 + I(z,t)/I_{\text{sat}}}. \tag{2.9}$$

Integrating both sides of the above equation, we obtain a perturbative equation to second order in time [2]:

$$\sigma_0 n = ln(I_0/I_f) + \frac{I_0 - I_f}{I_{\text{sat}}} + \frac{(k_{\text{r}}v_{\text{r}}t)^2}{3}\left(\frac{I_{\text{sat}}}{I_f + I_{\text{sat}}} - \frac{I_{\text{sat}}}{I_0 + I_{\text{sat}}} + \ln\left(\frac{I_f + I_{\text{sat}}}{I_0 + I_{\text{sat}}}\right)\right). \tag{2.10}$$

In Fig. 2b, we examine for what imaging times the above perturbative equation, as well as the modelt that completely ignores recoil induced detuning, is valid. We do this by performing numerical simulations to extract a value for the final intensity I_f and using Eq. 2.4 and Eq. 2.10 to extract values $\sigma_0 n$ that would be deduced from experimnet. We find that within the recoil time, both analytic expressions start to differ from the true atomic column density by over 5%, and the perturbative model of Eq. 2.10 quickly divereges thereafter.

In the following sections, we describe two versions of numerical simulations that we have performed in order to appropriately extract atomic column densities from experimental data.

2.5   Stationary atom model

In order to numerically simulate the imaging process, we assume a Gaussian distribution of atoms along the propagation direction, $\rho(z) = n/sqrt2\pi w e^{(}-z^2/2w^2)$. The dependence of the result on the choice of cloud width w is discussed in the next chapter. We divide the cloud into small bins along z. For the initial version of the simulation, the atoms were assumed to stay within the same bins for the entire duration of the imaging pulse, i.e. the cloud shape remained constant. We
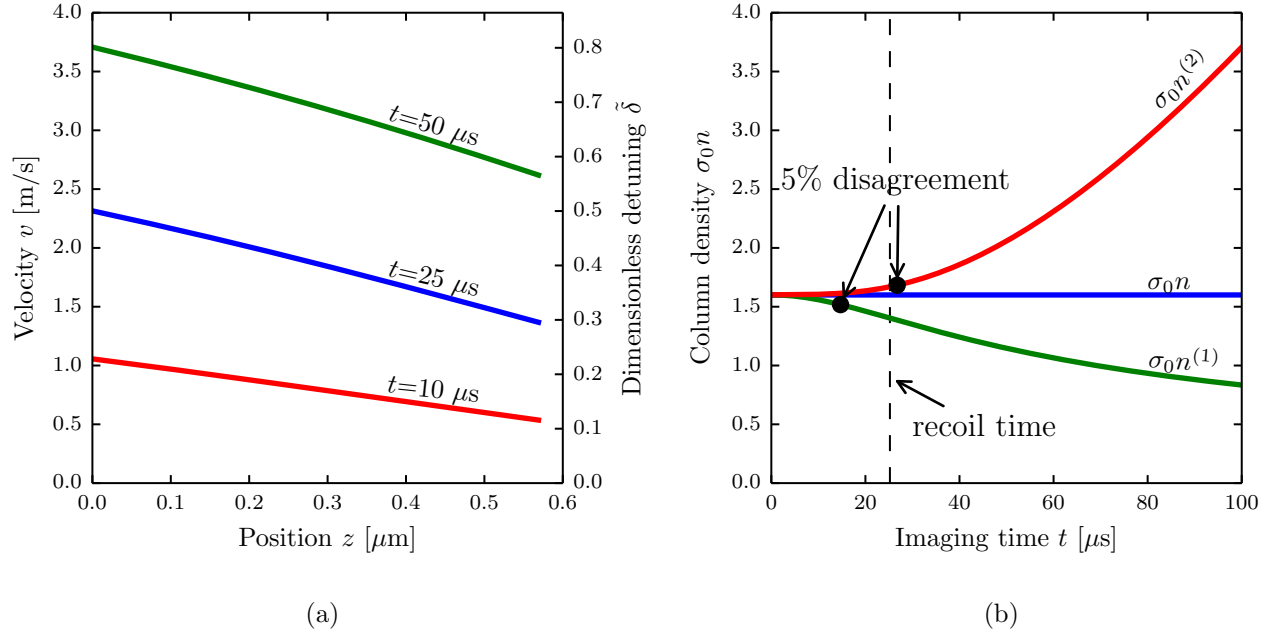
(a) (b)

Figure 2: (a) Dependence of velocity and detuning on position simulated for ^{40}K at three different imaging times and a probe intensity $\tilde{I}_0 = 0.8$. (b) Column densities deduced from optical depths obtained from recoil detuning corrected simulation of on-resonant imaging of ^{40}K atoms at probe intensity $\tilde{I}_0 = 0.8$. The input column density $\sigma_0 n = 1.6$. $\sigma_0 n^{(1)}$ is the high probe intensity corrected column density given by Eq. (2.4). $\sigma_0 n^{(2)}$ is the column density as expanded to second order in time, Eq. (2.10).

then used Eqs. 2.5-2.6 to numerically propagate the probe intensity and detuning as a function of both time and space. The algorithm used is detailed by Alg. 1.

Algorithm 1 Stationary atom model

$I[n = 0, t] = I_0$ {n is the bin index, t is the time index, I is in units of I_{sat}}
$\delta[n, t = 0] = 0$ {light initially resonant, δ in units of $\Gamma/2$}
$H_f = 0$ {Radiant fluence seen by camera after passing through cloud}
for $t = 0$ to t_f **do** {loop over time steps}
   for $n = 1$ to N **do** {loop over bins, N is total bin number}
     $A = \sigma_0 \rho[n] dz$ {dz is the size of spatial step}
     $B = v_r dt/(\hbar c \rho[n])$ {dt is the size of the time step}
     $I[n, t] = I[n - 1, t] - AI[n - 1, t]/(1 + \delta[n, t - 1]^2 + I[n - 1, t])$ {Eq. (2.5)}
     $\delta[n, t] = \delta[n, t - 1] + B(I[n - 1, t] - I[n, t])$ {Eq. (2.6)}
   end for
   $H_f = H_f + I[N, t]dt$ {collecting total fluence seen by the camera}
end for
$OD^{\text{sim1}} = -\ln(H_f/I_0 t_f)$

We call the optical depth obtained in this way OD^{sim1}, to distinguish if from the simulated optical depth via the method described in the next section.

The validity of this model can be checked by considering limits where the equations are analytically solvable. For short imaging times, the recoil-induced detuning should not contribute to the optical depth, and therefore Eq. 2.4 should become exact. This is seen in Fig. 3a, where the imaging pulse is only 3 μs long and the simulated optical depth (blue dots) agrees with that given by Eq. 2.4 for all intensity regimes.

Even at longer imaging times, the problem can be analytically solved for limits of both high and low intensity compared to the saturation intensity. At intensities $I \gg I_{\text{sat}}$, even far detuned atoms will scatter light at their maximum, and we can assume $\delta^2/\Gamma^2 \ll I/I_{\text{sat}}$, reducing back to Eq. 2.4. At extremely low intensities, atoms will scatter very little light and the detuning $\delta^2/\Gamma^2 \ll 1$, again reducing back to Eq. 2.4. As seen in Fig. 3 b,c the simulation agrees with the analytic Eq. 2.4 in the limit of both high and low intensities. But, as the imaging time increases, the disagreement due to recoil induced detuning grows.
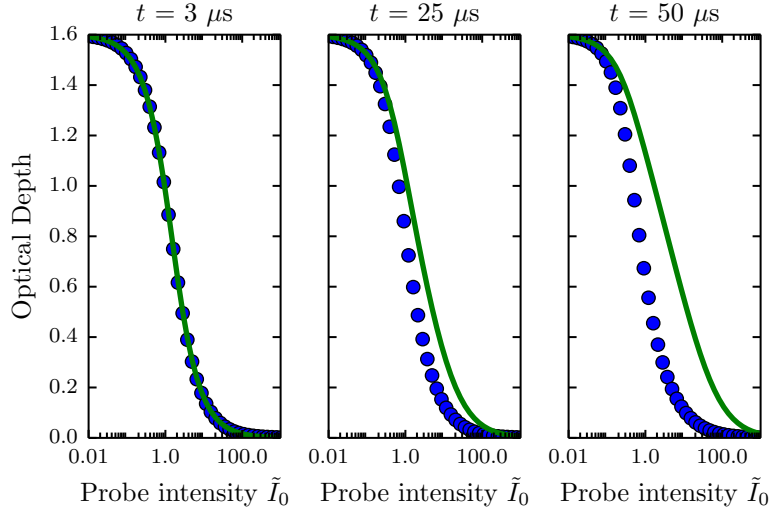
Figure 3: Optical depth as a function of probe intensity as predicted by the simulation (blue symbols) and by Eq. (2.4) (green curves), for three different imaging times. As expected, the predictions agree in both the high and low intensity limits, and differ for probe intensities comparable to the saturation intensity and longer imaging times.

The simulation allows us to extract both the intensity and the detuning as a function of both time and position. We can use this information to infer the velocity and therefore the displacement of the atoms during the imaging pulse, and check if our assumption that the atoms stay in their original 'bins' during the image pulse is valid. Figure 4a shows the position, deduced by integrating the recoil-induced velocity, as a function of time of the first, middle, and last spatial 'bin' for a probe intensity slightly above saturation, $I = 1.2 I_{\mathrm{sat}}$. As seen in the figure, not only do the atoms move beyond their 'bins', but also at long imaging times the first atoms (which have absorbed the most light) overtake the last ones. Therefore, the atomic cloud does not maintain shape during the imaging pulse, and our initial assumption is invalid.
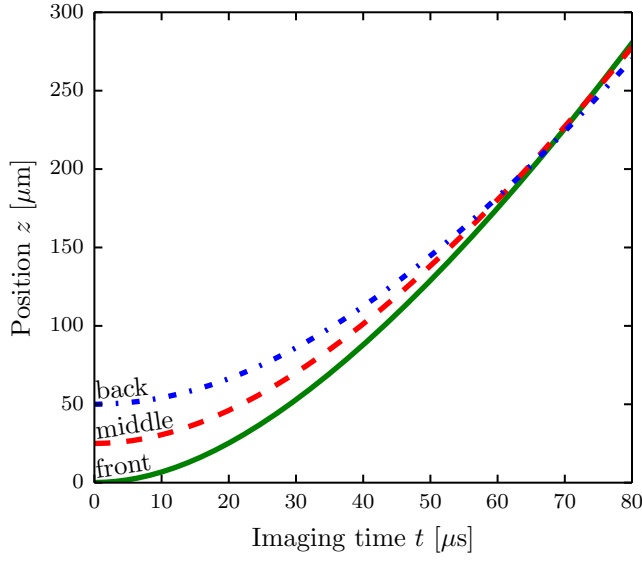
(a)
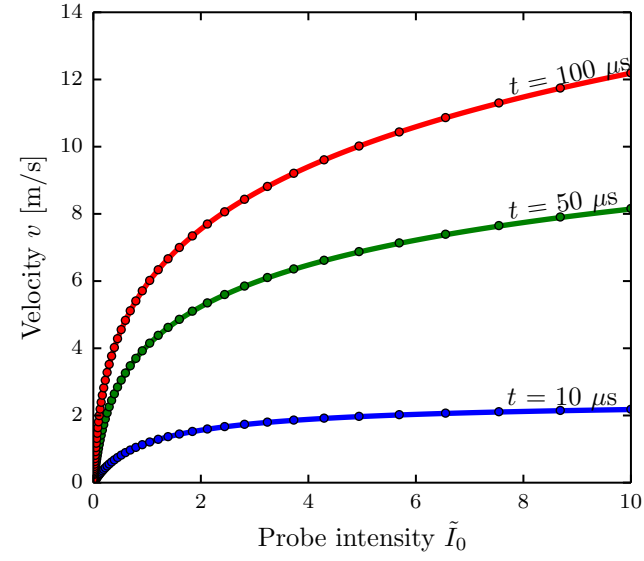
(b)

Figure 4: (a) Position of atoms as a function of imaging time for atoms in the first (solid green), middle (dashed red), and last (dotted blue) bins of the simulated density distribution for an initial cloud 50 μm in extent. The probe intensity used in this calculation was $1.2\,I_{\text{sat}}$, and the column density was $\sigma_0 n = 1.6$. (b) The velocity of a single composite atom as a function of probe intensity for various imaging times. Simulation data (dots) and numerical solutions of Eq. (2.11) (lines) are in agreement.

2.6   Traveling atom model

To model the recoil-induced detuning effect during the imaging pulse taking into account the potentially significant spatial displacement of the atoms, we performed a second version of our simulation. In this version, we clumped some number of atoms N_{ca} into a single composite atom, and then tracked the detuning, velocity and position of each composite atom as a function of imaging time. Tacking individual atoms would be computationally inaccessible for reasonable cloud sizes. The algorithm used is given by Alg. 2.

Algorithm 2 Travelling atom model

$z[n] = z_0$, $\delta[n] = 0$ {initialize position and detuning for each composite atom, labeled by index n}
$O[i] = n$ {make a list of composite atom indexes, ordered by position}
$I[n = 0, t] = I_0$ { t is the time index, I is in units of I_{sat}}
$H_f = 0$ {Radiant fluence seen by camera after passing through cloud}
for $t = 0$ to t_f **do** {loop over time steps}
  for $i = 1$ to N **do** {loop over superatoms}
    $n = O[i]$ {apply probe intensity to composite atoms in order of appearance}
    $A = \sigma_0 N_{sa} dz$ {dz is length over which atoms were grouped into single composite atom}
    $B = v_r dt/(\hbar c N_{sa})$ {dt is the time step}
    $I[n,t] = I[n-1,t] - AI[n-1,t]/(1 + \delta[n]^2 + I[n-1,t])$ {Eq. (2.5)}
    $\delta[n] \mathrel{+}= B\left(I[n-1,t] - I[n,t]\right)$ {Eq. (2.6), detuning in units of $\Gamma/2$}
    $z[n] \mathrel{+}= dt\Gamma\delta/2k$ {k is the wavenumber, $\Gamma\delta/2k$ is the velocity at δ detuning}
  end for
  $O[i]$=sort(n, key $=z[n]$) {sort composite atom indexes by current position}
  $H_f H_f + I[N,t]dt$ {collecting total fluence seen by the camera}
end for
$OD^{\mathrm{sim2}} = -\ln\left(H_f/I_0 t_f\right)$

To check the validity of this version of the simulation, we check the velocity of a composite atom as a function of time in an analytically solvable limit. In this case, we take the limit of a single composite atom, such that the intensity seen by the composite atom becomes time independent. This simplifies Eqs. 2.5 and 2.6 to only carry time dependence in the detuning term, and we can then plug Eq. 2.5
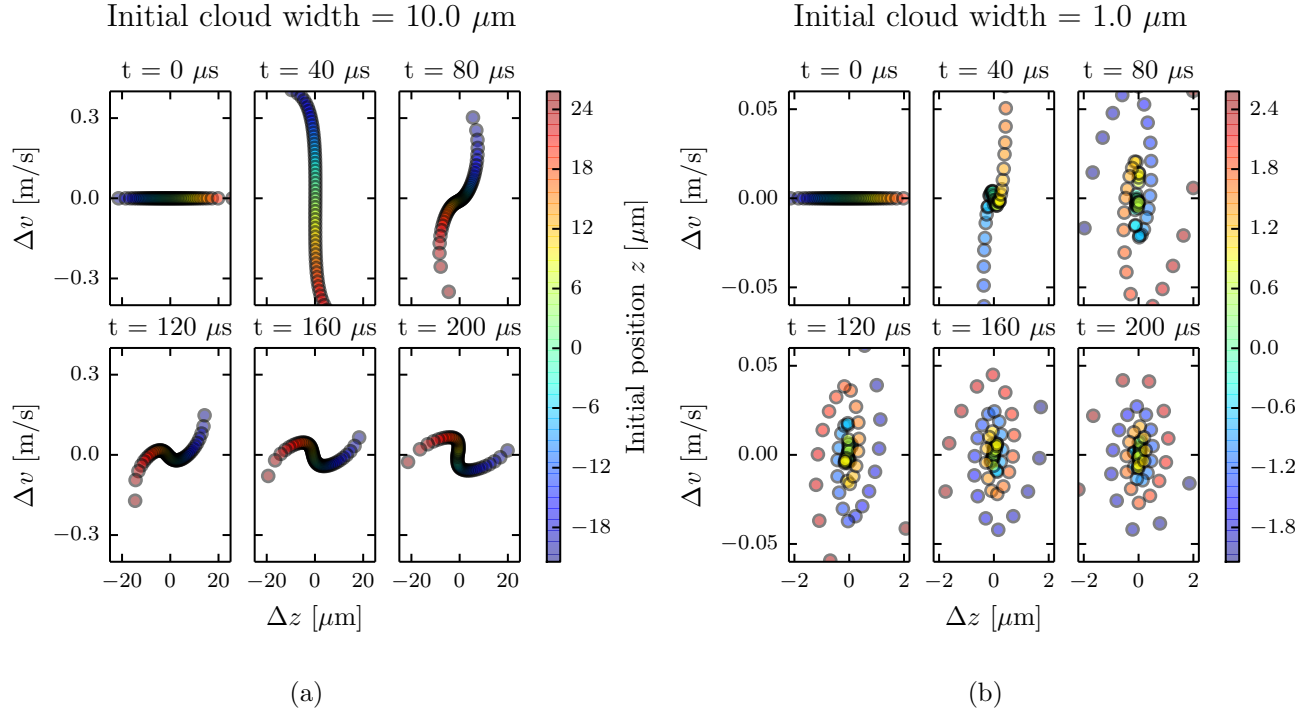
Figure 5: Phase space evolution of an atomic cloud exposed to probe light with intensity $\tilde{I}_0 = 1.2$. We defined $\Delta v = v - \langle v(t) \rangle$ and $\Delta z = z - \langle z(t) \rangle$, subtracting out the center of mass position and velocity of the cloud. The column density $\sigma_0 n$ is 1.6, and the initial cloud is a Gaussian with a width of 10 μm in (a) and 1 μm in (b). The center of mass velocities $\langle v \rangle$ are (0, 3.41, 5.26, 6.52, 7.50, 8.32) m/s sequentially, and are the same for both initial cloud widths.

into Eq. 2.6 and differentiate both sides with respect to time to obtain

$$\frac{d\delta(t)}{dt} = \frac{\Gamma k_r v_r}{2} \frac{I/I_{\text{sat}}}{1 + 4\delta^2/\Gamma^2 + I/I_{\text{sat}}}. \tag{2.11}$$

Equation (2.11) can be solved numerically, and is in agreement with our simulation, as seen in Fig. 4(b).

We then used this version of the simulation to look at the motion of composite atoms as a function of imaging time in phase space (ie, velocity and position). Some examples of this motion can be seen in Fig. 5. As seen in the figure, the atomic cloud is significantly distorted during the imaging pulse and the atoms perform some crazy acrobatics.

It remains to check how the atoms' acrobatics affect the resulting optical depth, ie the attenuation of the probe beam. To do this, we compare the optical depths generated by our stationary atom model, OD^{sim1}, and by our travelling atom model, OD^{sim2}. The results of this comparison are seen in Fig. 6(a). As seen from the figure, the optical depths predicted by the two versions of the simulation are negligibly small - $\left| OD^{\text{sim1}} - OD^{\text{sim2}} \right| / OD^{\text{sim1}} \leq 0.005$. We also checked the effect of having different initial distributions of atoms in space by varying the initial function $\rho(z)$ and keeping the total atom number constat. We found the effect of this to be negligible as well. Therefore, to infer atomic column densities from observed optical depths, it is sufficient to use the satationary atom model.

2.7   Calibration of saturation intensity

Saturation intensity is an intrinsic propety of the atom, so the idea of calibrating it may be confusing. However, there are several experimental parameters that may influence exactly what value of I_{sat} is appropriate to use in Eq. 2.5 and 2.6, such as losses in the imaging system and polarization of the probe beam. In addition, we have no direct experimental access to the total radiant fluence (time integral of intensity) seen by the camera. Instead, the light hitting the charge-coupled device (CCD) camera triggers some number of photoelectrons to be registered. The proportionality between the number of photons hitting the camera and the number of photoelectrons it triggers is called the quantum efficiency q_e of the camera. The number of these photelectrons, after some electronic gain and noise introduced during the readout process, is then read out as a number of 'counts' registered on each pixel. The camera-dependent factors influencing how the number of counts depends on the number of incoming photons can be convolved with the experimental factors of probe polarization and optical loss into a single calibration of the effective saturation intensity in units of 'counts' output by the camera per unit time.
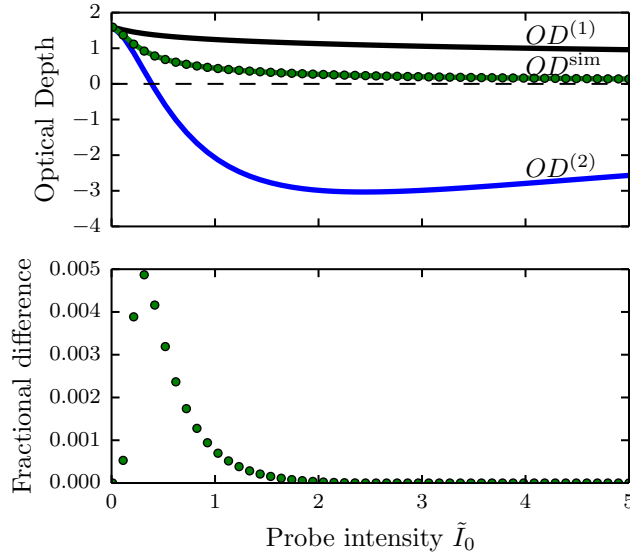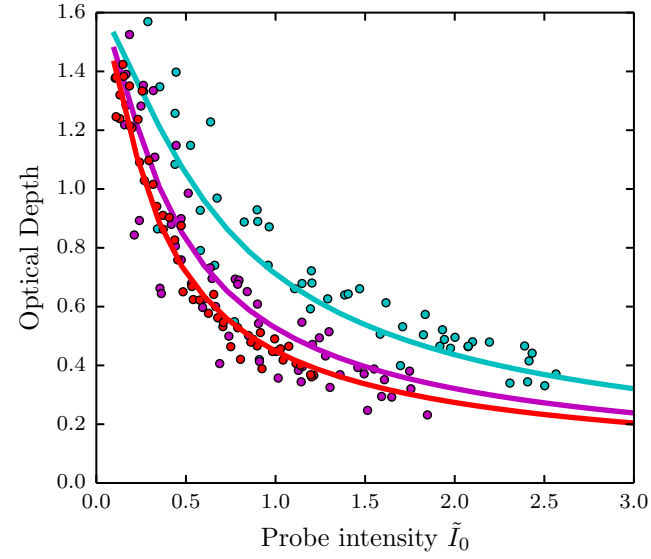
Figure 6: (a) Top. Optical depth as a function of probe intensity for an imaging time $t = 100$ μs. $OD^{(1)}$ and $OD^{(2)}$ are optical depths predicted from a given column density by Eq. (2.4) and (2.10) respectively. The two versions of simulated optical depth, OD^{sim1} (green curve) and OD^{sim2} (green dots) are plotted. Bottom. The fractional difference between two versions of the simulated OD, $\left|OD^{\mathrm{sim1}} - OD^{\mathrm{sim2}}\right|/OD^{\mathrm{sim1}}$. (b) The optical depth as a function of probe intensity for three imaging times: $t = 40$ μs (cyan), $t = 75$ μs (magenta), $t = 100$ μs (red). The dots represent experimental data and the lines represent the best fit of simulated data. The optimal fit parameters pictured are a $\sigma_0 n$ of 1.627(5) and saturation intensity of 29(7) counts/μs.

To calibrate this effective I_sat in camera counts per unit time, we absorption imaged our cloud of ^{40}K atoms for a range of probe intensities for three different values of imaging time: 40 μs, 100 μs, and 200 μs. We select a small region in the center of the cloud, where we can assume the atomic column density $\sigma_0 n$, and the initial probe intensity I_0 to be roughly constant. We then average the values of I_0 and I_f over this region and plot the final intensity I_f as a function of I_0. We then used the optical depth predicted by our simulation OD^sim and used that to simultaniously fit the three curves with I_sat and $\sigma_0 n$ as fit parameters, as shown in Fig. 6(b). As can be seen from the figure, this procedure not only allows us to read off I_sat in units of camera counts per μs, but also shows that our simulation accurately reproduces the differences in OD dependenc on imaging time.

2.8   SNR optimization

Using the simulations described in the previous sections, we can create a lookup table of atomic column densies as a function of initial and final probe intensities I_0 and I_f for any given imaging time. This lookup table can be then used to interpret experimental data and obtain the atom number in regimes where the recoil-induced detuning is significant. This procedure can also be used to propagate photon shot noise into uncertainty in measured atom number.

We consider Poisson distributed photon shot noise, converting into shot noise on photoelectrons triggered inside the CCD. The standard deviation will then be proportional to $q_\text{e}\sqrt{N_p}$, where q_e is the quantum efficiency of the camera and N_p is the photon number. This uncertainty can be then propagated via the lookup table into uncertainty on the measured atomic column density $\delta_{\sigma_0 n}$. The signal to noise ratio (SNR) can then be expressed as $\sigma_0 n / \delta_{\sigma_0 n}$.
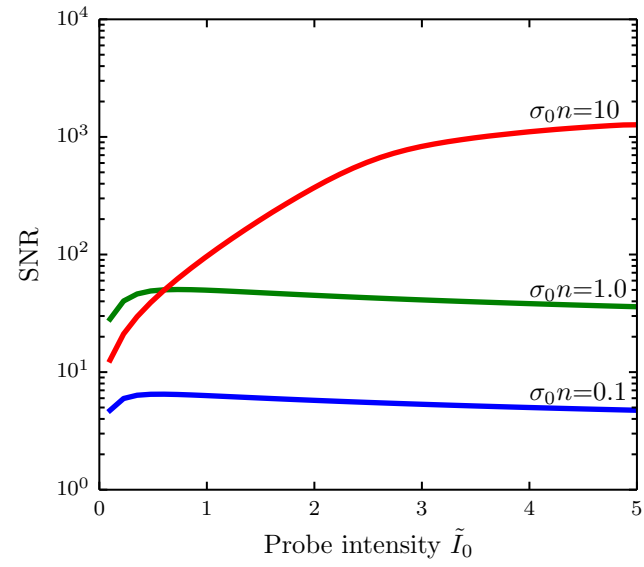
We study the SNR as a function of imaging time and initial probe intensity for a few different atomic column densities. Some representative data is shown in

Fig. 7. As seen in Fig. 7(a), for a wide range of atomic column densities, extending the imaging time beyond 40 μs no longer yields significant improvements in SNR. There is, however, a factor of 1.5 improvement between using an imaging time of 10 μs, where the simple model given by Eq. 2.4 is appropriate, and 40 μs. Therefore, there are signifiant gains that can be made by going to longer imaging times and making use of the simulated lookup table.

This simulation allowed us to interpret experimental data. For a given imaging time, we created a look-up table of predicted optical depth as a function of probe intensity and atomic column density. We then found the observed optical depth on this table, with the given probe intensity, and inferred the atomic density. The uncertainty in the measured intensities can be propagated through this procedure, and we established optimal imaging parameters to maximize the SNR of this detection scheme. Figure 7(b) illustrates that the optimal initial probe intensity is different for different atom numbers. For low atom numbers, $\sigma_0 n \approx 0.1$, a probe intensity of $I_0 \approx 0.6 I_{\text{sat}}$ is best.
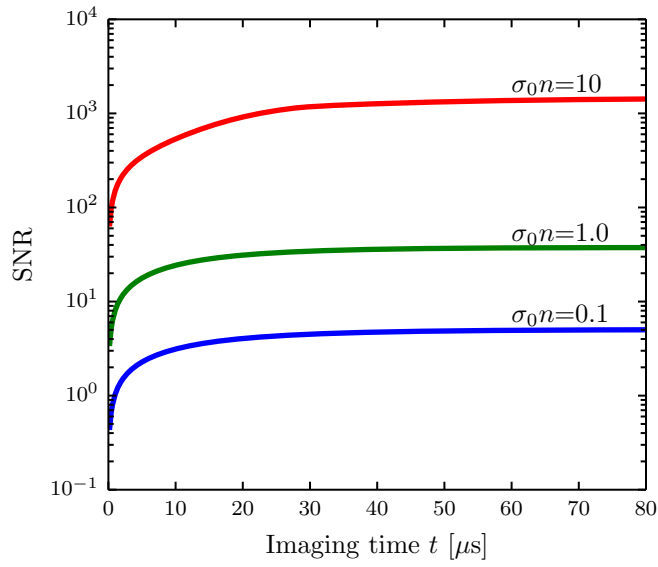
Figure 7: SNR for three different column densities after correcting for recoil induced detuning. (a) SNR as a function of imaging time for a probe intensity of $\tilde{I}_0 = 5.0$ and (b) SNR as a function of probe intensity for an imaging time of 50 μs.

Chapter 4:   Synthetic dimensional lattice

In this chapter we explain the idea of an effective 2-D lattice with one real dimension created by lattice cites of a 1-D optical lattice and one 'synthetic' dimension created by treating the internal spin states of the atom as sites along a transverse axis. We do this by treating each dimension individually first. In the section 4.1, we describe 1-D optical lattices. We exlain the far off resonant interaction that leads to the AC Stark shift, and use it to write down the 1-D optical lattice Hamiltonian. We describe the often used tight binding approximation of the lattice Hamiltonian. We describe how the lattice is calibrated in our lab, and introduce Bloch oscillations.

In section 4.2, we describe the hyperfine structure of Rubidium, used as sites in the 'synthetic' dimension. We then describe two methods for coupling them to introduce tunneling in the synthetic dimensions: rf and Raman transitions. We describe the calibration procedures, and show ground states of the system with each of the couplings applied. In the last section, we combine the two dimensions and write out the full synthetic dimensions Hamiltonian. We plot the band structure, and describe the emergence of the effective magnetic field. We show the calibration procedure, and show the ground states of the system, featuring both bulk and edge satates with narrowing due to the magnetic length. We then show skipping orbits created by loading a superposition of states on the edge of the system, analagous to edge magnetoplasmons. The experiments in this section were detailed in the publication [3].

4.1 One dimensional optical lattices

The first, 'real' dimension in the synthetic dimensional lattice is discretized into sites by an optical lattice. Optical lattices are a staple of cold atomic physics, and are commonly used to emulate the crystal structure present in metals and other condensed matter systems. In this section, we describe the orgin of the periodic potential, derive the Hamiltonian and show how the lattice depth is detected and calibrated in the lab.

4.1.1 Far off-resonant atom-light interaction

As described in section 2.1, on timescales where spontaneous emission can be neglected, two-level atoms exposed to laser radiation undergo coherent Rabi oscillations between the two levels. Starting with c_g and c_e as the time-dependent coefficients multiplying the eigenstate wavefuntions of the ground and excited state respectively, and assuming the atom starts in the ground state $c_g(t = 0) = 1$, we make the traditional transformation to the rotating frame:

$$c'_g(t) = c_g(t) \tag{4.1}$$

$$c'_e(t) = c_e(t)e^{-i\delta t}, \tag{4.2}$$

where δ is the detuning of laser light from resonance. In this frame, we can write the atom-light Hamiltonian in the $\begin{pmatrix} c'_g \\ c'_e \end{pmatrix}$ basis as:

$$H = \hbar \begin{pmatrix} -\delta/2 & \Omega/2 \\ \Omega/2 & \delta/2 \end{pmatrix}, \tag{4.3}$$

where Ω is the coupling strength, also known as the Rabi frequency. In the limit of no coupling, $\Omega = 0$, in the rotating frame the eigenenegies are $E_\pm = \pm\hbar\delta/2$. For non-zero coupling, finding the eigenvalues of H gives $E_\pm = \pm\hbar\sqrt{\delta^2 + \Omega^2}/2$. Therefore, the bare (without light) eigenenrgies are shifted in the presence of the light.

For a far detuned laser beam, one expects that no absorption of the light will actually take place, and the atom will remain entirely in the ground state. Indeed, solving the Shroedinger equation with the above Hamiltonian

$$i\hbar\frac{d}{dt}\begin{pmatrix} c'_g \\ c'_e \end{pmatrix} = H\begin{pmatrix} c'_g \\ c'_e \end{pmatrix} \tag{4.4}$$

we obtain the oscillating excited state population

$$c'_e(t) = -i\frac{\Omega}{\sqrt{\Omega^2 + \delta^2}}\sin\left(\frac{\sqrt{\Omega^2 + \delta^2}t}{2}\right), \tag{4.5}$$

where the amplitude of the oscillation approches zero in the limit $\Omega \ll \delta$. Thus, the only effect of the light in this regime is to shift the eigenenergies of the ground and excited states. Expanding the energies in the small parameter Ω/δ, we obtain the shifted energies $E_\pm = \pm\hbar\sqrt{\delta^2 + \Omega^2}/2 \approx \pm(\delta/2 + \Omega^2/4\delta)$. The shift from bare energy levels is thus

$$\Delta E_\pm = \pm\Omega^2/4\delta. \tag{4.6}$$

This laser intensity dependent energy shift is called the AC Stark shift, and is the basis of most laser created potentials for cold atoms.

For the ground state, and a red detuned laser beam (where the laser frequency is lower than the resonant frequency), this creates energy minima in locations of maximal laser intensity. For the lattice described in this chapter, as well as for the trapping of our atoms in the final stages of cooling, we use high power (up to 10 W)

lasers with wavelength $\lambda_L = 1064$ nm.

4.1.2   Lattice Hamiltonian

Our 1-D optical lattice is created by retro-reflecting the $\lambda_L = 1064$ nm laser, creating a standing wave of light. Via the AC Stark shift, this creates a periodic potential for the atoms of the form

$$V = V_0\sin^2(k_L x), \tag{4.7}$$

where $k_L = 2\pi/\lambda_L$ is the wavenumber associated with the lattice recoil momentum. The time-independent Hamiltonian, for some eigenenergy E_n, will be given by

$$-\frac{\hbar^2}{2m}\frac{d^2}{dx^2}\Psi_n(x) + V_0\sin^2(k_L x)\Psi_n(x) = E_n\Psi_n(x). \tag{4.8}$$

Since the potential is spatially periodic, we can invoke Bloch's theorem [?]:

$$\Psi_{n,q} = e^{iqx}u_{n,q}(x), \tag{4.9}$$

where q is the crystal momentum restricted to $\pm\hbar k_L$, and $u_{n,q}(x)$ is the spatially varying part of the wavefunction. Plugging this in to the Hamiltonian, we obtain

$$-\frac{\hbar^2}{2m}\left(-q^2 + 2iq\frac{d}{dx} + \frac{d^2}{dx^2}\right)u_{n,q}(x) + V_0\sin^2(k_L x)u_{n,q}(x) = E_n u_{n,q}(x). \tag{4.10}$$

Expanding $u_{n,q}(x)$ in Fourier components commensurate with the lattice period of $2k_L$ as $u_{n,q}(x) = \sum_{j=-\inf}^{\inf} a_j e^{i2k_L jx}$, we obtain

$$\sum_j\left(\frac{\hbar^2}{2m}(q + 2k_L)^2 a_j + V_0\sin^2(k_L x)a_j\right)e^{i2k_L jx} = E_n\sum_j a_j e^{i2k_L jx}. \tag{4.11}$$

Re-writing $\sin^2(k_L x) = (e^{-2ik_L x} + e^{2ik_L x} - 2)/4$, multiplying both sides by $e^{i2k_L j' x}$ and invoking $\sum c_j e^{ik(j-j')} = \delta_{jj'}$, where $\delta_{jj'}$ is the Kroniker delta and c_j are appropriately normalized coefficients, we get for any value of the index j

$$\frac{\hbar^2}{2m}(q + 2k_L j)^2 a_j - \frac{V_0}{4}(a_{j+1} + a_{j-1}) = E_n a_j. \tag{4.12}$$

This can be expressed in matrix form

$$H_L = \begin{pmatrix} \ddots & & & & & \\ & \frac{\hbar^2}{2m}(q+4k_L)^2 & \frac{V_0}{4} & 0 & 0 & 0 \\ & \frac{V_0}{4} & \frac{\hbar^2}{2m}(q+2k_L)^2 & \frac{V_0}{4} & 0 & 0 \\ & 0 & \frac{V_0}{4} & \frac{\hbar^2}{2m}q^2 & \frac{V_0}{4} & 0 \\ & 0 & 0 & \frac{V_0}{4} & \frac{\hbar^2}{2m}(q-2k_L)^2 & \frac{V_0}{4} \\ & 0 & 0 & 0 & \frac{V_0}{4} & \frac{\hbar^2}{2m}(q-4k_L)^2 \\ & & & & & & \ddots \end{pmatrix}, \tag{4.13}$$

in the basis of momentum orders $|k\rangle = e^{ikx}$ given by:

$$\begin{pmatrix} \vdots \\ |q + 4k_L\rangle \\ |q + 2k_L\rangle \\ |q\rangle \\ |q - 2k_L\rangle \\ |q - 4k_L\rangle \\ \vdots \end{pmatrix}. \tag{4.14}$$

This matrix can be diagonalized for every value of the crystal momentum q, with some examples shown in Figure [ADD BAND STRUCTURE FIGURE]. It is convenient to define the lattice recoil energy $E_L = \hbar^2 k_L^2 / 2m$. Then, we can re-write

the Hamiltonian with V_0 in units of E_L and momenta q in units of k_L as

$$H_L/E_L = \begin{pmatrix} \ddots & & & & & \\ & (q+4)^2 & \frac{V_0}{4} & 0 & 0 & 0 \\ & \frac{V_0}{4} & (q+2)^2 & \frac{V_0}{4} & 0 & 0 \\ & 0 & \frac{V_0}{4} & q^2 & \frac{V_0}{4} & 0 \\ & 0 & 0 & \frac{V_0}{4} & (q-2)^2 & \frac{V_0}{4} \\ & 0 & 0 & & \frac{V_0}{4} & (q-4)^2 \\ & & & & & & \ddots \end{pmatrix}. \qquad (4.15)$$

In any numerical simulation, the number of momentum orders that can be included is finite. We determine the value of the parameter $n = \max(|j|)$ as the lowest n at which the eigenvalues stop changing to machine precision from $n-1$. The code for finding and plotting the eigenvalues and eigenvectors of the lattice hamiltonian is included in Appendix [MAKE APPENDIX WITH CODE?].

4.1.3   Tight binding approximation

In the limit of large lattice depths, $V_0 >\approx 5E_L$, the lattice Hamiltonian is well approximated by the tight-binding model. In the tight binding model, the basis is assumed to be a set of orthogonal functions, called Wannier functions, localized to each lattice site $|j\rangle$. The approximation lies in assuming only nearest neighbor tunnelings between the sites, forming the tight-binding Hamiltonian

$$H_{\text{tb}} = -t\,|j\rangle\,\langle j+1| + \text{H.c.}, \qquad (4.16)$$

where t is the tunneling amplitude between nearest neighbor sites and H.c. stands for Hermitian conjugate. We have neglected the diagonal kinetic energy term, as it will be equal for every Wannier function $|j\rangle$ and thus represents a constant energy

offset. All the information about the lattice depth is therefore reflected in the tunneling amplitude t.

The tight binding Hamiltonian can also be expressed in the momentum basis by Fourier transforming the basis functions:

$$|j\rangle = \frac{1}{\sqrt{N}} \sum_{k_j} e^{-ik_j j} |k_j\rangle, \tag{4.17}$$

giving the Hamiltonian

$$H_{\text{tb}} = -\frac{1}{N} \sum_{k_1} \sum k_2 t e^{-ijk_1} e^{ik_2(j+1)} |k_1\rangle \langle k_2| + \text{H.c} = 2t\cos(k) |k\rangle \langle k|. \tag{4.18}$$

From this we can directly read off the band structure of the tight binding Hamiltonian. First, we notice that we only obtain one band - to approximate higher bands with the tight binding approximation we would need to construct a different set of Wannier functions and a different tunneling strength. Second, we see that the lowest band is simply a cosine - therefore we have solved for the band structure without even defining what the basis Wannier functions are! Third, the amplitude of the cosine function is given by the tunneling strength t. This gives us a good clue as to how to determine the appropriate tunneling given a lattice depth V_0 - [FIND EXPRESSION FOR AMPLITUDE OF LOWEST BAND COSINE AT LARGE V0] simply find a t that matches the amplitude of the lowest band.

The precise form of the Wannier functions depends on both the depth of the lattice and the band being reproduced. It is not necessary for us to find their full expression, as the band structure can be calculated without them. The most commonly used definition, however, is

$$|j\rangle = \int_{\text{BZ}} e^{iqja} \Psi_q(x) \text{d}q, \tag{4.19}$$

where the integral is over the Brillouin zone, from $-k_L$ to k_L, a is the lattice spacing $\lambda_L/2$, and Ψ_q is the Bloch wavefunction at crystal momentum q.

4.1.4 Pulsing vs adiabatic loading of the lattice

The lattice depth parameter $V_0/4$, for a range of values, can be well calibrated experimentally by pulsing on the lattice. Here, the word pulsing indicates that the lattice is turned on fully non-adiabatically, if not instantaneously, such that the original bare momentum state is projected onto the lattice eigenbasis. If the atoms start out stationary in the trap, the bare state in the momentum basis is simply

$$|\Psi_0\rangle = \begin{pmatrix} \vdots \\ 0 \\ 0 \\ 1 \\ 0 \\ 0 \\ \vdots \end{pmatrix}. \tag{4.20}$$

Since the lattice eigenbasis is distinct from the bare one, this will necessarily excite the atoms into a superposition of lattice eigenstates, each evolving with a different phase according to the eigenenergy while the lattice is on. Then, when the lattice is snapped back off, the wavefunction is projected back into the bare basis, and the varying phase accumulation results in a beating of the different momentum orders. This can be calculated simply by using the time evolution operator

$$|\Psi(t)\rangle = e^{-iH_L t/\hbar} |\Psi_0\rangle. \tag{4.21}$$

By pulsing on the lattice for variable amounts of time t, we can obtain fractional

populations in the different momentum states. Time-of-flight imaging captures the momentum distribution of the cloud, and the different entries of $\Psi(t)$ in the momentum basis will thus appear as different clouds on the absorption image [IN-CLUDE IMAGES FROM PULSING DATA]. The fractional population in these clouds corresponds to a measurement of $|a_j|^2$. Typically for our values of the lattice depth $V_0 < 10E_L$, it is sufficient to simply count three central momentum orders, $k = q, q \pm 2k_L$. Then, we can fit Eq. 4.21 to the data with fitting parameter V_0, thus deducing the lattuce depth. Some examples of these pulsing experiments are presented in figure [MAKE FIGURE]:

In contrast to pulsing, adiabatic loading turns the lattice on slowly, such that the atomic wavefunction starting in the bare ground state can continuously adjust to remain in the ground state of the current Hamiltonian, without projecting onto any of the higher bands. The adiabatic timescale depends on the spacing between the ground and next excited band (or if starting in a different eigenstate, the nearest eigenstate). If the energy difference between the ground and first excited state is ΔE, the timescale on which the lattice is turned on must fullfill $t \gg h/\Delta E$.

[FIND PICTURES OF ADIABATICALLY LOADED LATTICE STATES]

4.2 Raman and rf coupling

The second, 'synthetic' dimension in the effectively 2-D lattice is formed by the internal hyperfine states of the atoms, forming sites along a second dimension. To induce tunneling along the synthetic sites, analogous to lattice hopping between neighboring sites, we must engeneer some coupling between them. There are two ways we induce this tunneling - with rf coupling, tuned to be directly resonant with the energy difference between the hyperfine levels, and with two-photon Raman coupling, tuned such that the energy difference between the two photons matches the hyperfine splitting. In this section we describe the hypefine structure of ^{87}Rb,

derive the Hamiltonians for both rf and Raman coupled states, and show how the Raman and rf coupled states are measured and calibrated in the lab.

4.2.1 Hyperfine structure

4.2.2 Raman and rf coupling Hamiltonians

4.2.3 Adiabatically loaded Raman and rf dressed states

4.3 Synthetic dimensions

4.3.1 Lattice Hamiltonian with Raman coupling

4.3.2 Emergence of effective magnetic field

4.3.3 Eigenstates of the synthetic 2-D lattice

4.3.4 Observation of skipping orbits

Bibliography

[1] H.J. Metcalf and P. van der Straten. *Laser Cooling and Trapping.* Graduate Texts in Contemporary Physics. Springer New York, 1999.

[2] Lindsey J. LeBlanc. *Exploring many-body physics with ultracold atoms.* PhD thesis, University of Toronto, 2011.

[3] B. K. Stuhl, H.-I. Lu, L. M. Aycock, D. Genkina, and I. B. Spielman. Visualizing edge states with an atomic bose gas in the quantum hall regime. *Science*, 349(6255):1514–, Sep 2015.